IEEE Access
Multidisciplinary ⋮ Rapid Review ⋮ Open Access Journal

Received 23 February 2023, accepted 10 April 2023, date of publication 12 April 2023, date of current version 19 April 2023.

Digital Object Identifier 10.1109/ACCESS.2023.3266641

RESEARCH ARTICLE

Near-Field Millimeter-Wave Imaging via Multi-Plane MIMO Arrays

GUANGNAN XING[1], SHIYONG LI[1], (Senior Member, IEEE), AHMAD HOORFAR[2], (Life Fellow, IEEE), QIANG AN[3], AND GUOQIANG ZHAO[1]

[1]Beijing Key Laboratory of Millimeter Wave and Terahertz Technology, Beijing Institute of Technology, Beijing 100081, China
[2]Antenna Research Laboratory, Center for Advanced Communications, Villanova University, Villanova, PA 19085, USA
[3]Department of Biomedical Engineering, Fourth Military Medical University, Xi'an 710032, China

Corresponding author: Shiyong Li (lisy_98@bit.edu.cn)

This work was supported by the National Natural Science Foundation of China under Grant 62071043.

ABSTRACT Multiple-input multiple-output (MIMO) array-based millimeter-wave (MMW) imaging has broad application prospects in concealed weapons detection due to its capability of high resolution at a reasonable cost. This paper presents a novel multi-plane MIMO array topology for near-field MMW imaging. The multi-plane MIMO arrays can offer wider angular observations of the target under test than the traditional planar MIMO arrays. Although the cylindrical MIMO array can achieve similar focusing performance as the multi-plane one, the multi-plane MIMO arrays are much easier to fabricate since each subarray has the same structure as a planar one. In addition, to speed up the image reconstruction process, we propose a corresponding three-dimensional (3-D) imaging algorithm with hybrid processing in the time-domain and wavenumber-domain. The proposed algorithm is even more efficient than the wavenumber-domain algorithm for the cylindrical MIMO array that has the same scale as the proposed multi-plane array scheme, which clearly shows that the hybrid time-wavenumber domain processing can avoid the enormous computation burdens of higher dimensional processing of the wavenumber-domain MIMO imaging algorithms. Numerical simulations and experimental results are provided to demonstrate the superiority of the proposed multi-plane MIMO array imaging technique in comparison with the most commonly used arrays and algorithms.

INDEX TERMS Multiple-input multiple-output (MIMO), multi-plane array, hybrid processing, time-domain, wavenumber-domain.

I. INTRODUCTION

MILLIMETER-WAVE (MMW) imaging can provide high resolution of the targets under test due to utilization of high frequencies and large signal bandwidth. In addition, MMW can penetrate some ordinary materials without health hazards at moderate power levels. Therefore, it has been widely applied in various areas including remote sensing [1], [2], non-destructive testing [3], [4], biomedical diagnosis [5], [6],and personnel security inspection [7], [8], to name a few.

The down-range resolution of a three-dimensional (3-D) imaging scheme is determined by the bandwidth of the working electromagnetic (EM) waves, while the cross-range resolutions along the horizontal and vertical directions are obtained through the use of a large antenna aperture [9]. Traditionally, by exploiting the synthetic aperture radar (SAR) technique, a 2-D antenna aperture can be realized by moving a 1-D antenna array along its perpendicular direction [10], [11]. However, mechanical scanning takes a relatively long time and is not well-suited for practical in-field operation. To meet the requirements of real-time data acquisition, one solution is to adopt the scheme of 2-D monostatic arrays with the full Nyquist samplings; this will, however, result in a huge number of antennas making the system costly and unaffordable.

In this respect, the multiple-input multiple-output (MIMO) array is a good choice for near-field fast MMW imaging as it employs all the possible combinations of transmit and receive

The associate editor coordinating the review of this manuscript and approving it for publication was Hasan S. Mir.

antenna elements to achieve a larger number of efficient phase centers, so as to reduce the overall system cost [12], [13]. Also, the MIMO array can offer the merit of reducing ghosts in radar images induced by multipath reflections [14]. Theoretically, MIMO systems only need one snapshot of data acquisition to form the image through employing orthogonal waveforms [15], [16]. In addition, most of the MIMO-based systems for near-field imaging work in a time-division multiplexing mode to further reduce system cost [17], [18], which also exhibits the virtue of better signal separation. Due to these advantages, MIMO systems have been widely employed in many radar applications, such as direction of arrival (DOA) estimation [19], [20], target detection [21], and multimode imaging [22].

This paper focuses only on the research of 2-D MIMO array-based imaging, which eliminates the mechanical scanning for a 3-D imaging scenario. The focusing properties of several representative 2-D MIMO array topologies, including the rectangular and Mills Cross arrays, were investigated in [23] for ultrasound imaging. A fully electronic MIMO array constructed by square clusters was proposed in [24], where the digital-beamforming technique was employed for image reconstruction. The fast imaging algorithm implemented in the wavenumber-domain was proposed in [25] for 2-D MIMO arrays with uniformly spaced antennas. An improved version of this algorithm, referred to as transverse spectrum deconvolution range migration, was considered in [26]. A range enhancement imaging technique based on the range migration algorithm (RMA) for MIMO planar array was proposed in [27]. The imaging performance of a nonuniform MIMO array based on the minimum redundancy criterion was demonstrated in [28]. A nonuniform fast Fourier transform (NUFFT)-based range migration algorithm was presented in [29] for a 2-D irregular MIMO array scheme. In [30], a precise wavenumber-domain algorithm was proposed for the cross MIMO array topology. Álvarez et al. in [31] provided the parallelizable Fourier-based imaging algorithms for the planar multistatic array-based systems. For real-time concealed threat detection, a fast imaging approach that transforms the MIMO data into the equivalent monostatic data using a phase calibration method was presented in [32]. Although the multistatic-to-monostatic correction provided an efficient imaging solution, this phase calibration also introduced an approximation which deteriorates the quality of imaging results.

The aforementioned arrays have a common property of forming a planar aperture, the observation angles of which are limited for the personnel imaging scenario. Large observation angles are usually essential to reduce the probability of missed detection for the safety inspection. The famous ProVision systems, originally from L3Harris now belonging to Leidos [33], employ a linear array associated with a circular-arc mechanical scanning to enlarge the observation angles of the human body. To improve the efficiency of image reconstruction, a modified Omega-K algorithm was proposed in [34] for a mechanical scanning MIMO arc array using

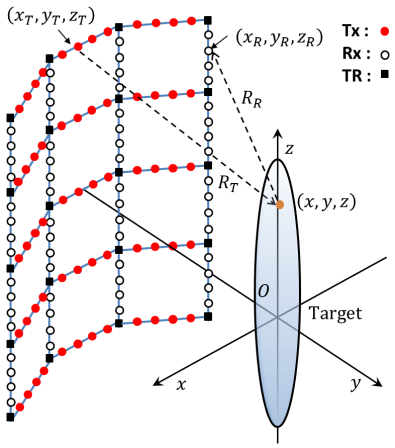

FIGURE 1. The imaging geometry of the multi-plane MIMO array topology.

the single-frequency data. An ultra-wideband imaging system was developed in [35] for whole body imaging, where the prototype system was illustrated with multi-plane array apertures. The antennas were configured at nonuniform positions and an iterative imaging technique was developed based on the back projection algorithm. Considering increasing the observation angles, a portable microwave imaging system was presented in [36]. The system is capable of real-time imaging with the help of GPUs, so it can be arbitrarily moved along the target under test. The information from different scanning positions was finally merged based on the multiview synthetic aperture imaging. However, this scheme takes a lot of time to acquire the data by moving the scanner manually. A cylindrical MIMO array topology without mechanical scanning was presented in [37] and [38], which can offer large observation angles with respect to the target and save much time for data acquisition. However, the fabrication of a cylindrical MIMO array is more complicated than that of a planar one. On the other hand, the proposed imaging algorithm in [38] for cylindrical MIMO array, named cylindrical range migration algorithm (cylindrical RMA), requires large memory usage and heavy computation burden due to the higher dimensional processing. Therefore, a novel more efficient imaging technique is in great demand to reconstruct the high resolution images of the target in the near-field.

As an approximation of the cylindrical aperture, the multi-plane aperture can also steer the antenna beams almost toward the target center and provide uniform illumination of the target area. In [39] and [40], a polyline shaped array scheme has been developed to approximate the circular-arc array, associated with mechanical scanning to realize 3-D imaging. In this paper, we extend the polyline array to a multi-plane MIMO array topology, as shown in Fig. 1, which consists of squared planar subarrays with identical structure and can provide wider observation angles than a planar MIMO array. In each squared subarray, the transmit antennas (denoted by "Tx") and receive antennas (denoted by "Rx") are uniformly arranged in a fully sampled manner along the two horizontal sides and two vertical sides (or vice versa), respectively. The "TR" elements located at the

intersections in Fig. 1 represent the antenna elements that act as transceivers, which can be just removed in practice for easy fabrication. The topology is formed by connecting each squared subarray next to one another along the horizontal and vertical directions, with antennas shared by the two adjacent subarrays. The proposed muti-plane MIMO array is more suitable for imaging of the human body, which can offer larger observation angles and achieve better imaging performance than the planar aperture. Additionally, the proposed array scheme is much easier to fabricate through using planar subarrays, which can reduce the system cost significantly compared to the cylindrical aperture.

Unlike the planar or cylindrical MIMO arrays, there is no existing efficient imaging algorithm to deal with such a multi-plane MIMO array scheme, except for the back-projection (BP) algorithm [41], however, with much higher computational complexity. To overcome the time-consuming problem of BP, we develop an imaging algorithm with hybrid processing in the time-domain and the wavenumber-domain for this multi-plane MIMO array topology. Specifically, we process the data in the wavenumber-domain along the vertical direction, while applying the time-domain processing along the horizontal and down-range directions of the multi-plane MIMO array. In so doing, we can achieve much faster imaging speed than using the BP algorithm. Compared to the cylindrical RMA, the proposed algorithm in this paper has even higher computational efficiency since it avoids the higher dimensional processing by taking advantage of the coherent sum-based processing along the polyline array dimension. In conclusion, the proposed multi-plane MIMO array imaging technique is novel both in terms of the array topology and the use of an efficient imaging algorithm for the practical application of concealed weapons detection, which can offer better imaging performance than the planar or the cylindrical MIMO arrays.

The rest of the paper is organized as follows. In the next section, we formulate the 3-D hybrid time-wavenumber domain imaging algorithm and discuss the details of the algorithm implementation. The resolutions and inter-element spacings of the multi-plane MIMO array are also outlined. Section III verifies the focusing performance and computational efficiency of the proposed imaging technique through simulations and experimental results. Section IV provides a summary of this paper.

II. MMW IMAGING VIA MULTI-PLANE MIMO ARRAY

A. FORMULATIONS

The imaging geometry of the multi-plane MIMO array is illustrated in Fig. 1. The coordinates of the transmit and receive antennas are denoted by $(\vec{r}_T, z_T)$ and $(\vec{r}_R, z_R)$ with $\vec{r}_T=(x_T, y_T)$ and $\vec{r}_R=(x_R, y_R)$ respectively. Under the first-order Born approximation [42], the scattered waves from a target with reflectivity $g(x, y, z)$ are given by,

$$s(\vec{r}_T, \vec{r}_R, z_T, z_R, k) = \iiint g(x, y, z) e^{-jk(R_T+R_R)} dxdydz, \tag{1}$$

where $k = \frac{2\pi f}{c}$ is the wavenumber, f represents the operational frequency, and c denotes the speed of light. R_T and R_R are, respectively, the distances from the transmit antenna to the target and from the target to the receive antenna, which can be expressed by,

$$R_T = \sqrt{\rho_T^2 + (z - z_T)^2}, \tag{2}$$

$$R_R = \sqrt{\rho_R^2 + (z - z_R)^2}, \tag{3}$$

where

$$\rho_T = \sqrt{(x - x_T)^2 + (y - y_T)^2}, \tag{4}$$

and

$$\rho_R = \sqrt{(x - x_R)^2 + (y - y_R)^2}, \tag{5}$$

Though the transmit and receive antennas are uniformly spaced on the multi-plane aperture, their distributions along the horizontal and down-range directions are nonuniform, which brings difficulty to the implementation of the Fourier transforms with respect to x and y. Fortunately, the antennas are uniformly spaced along the vertical direction. Therefore, based on the characteristic of this multi-plane MIMO array, we propose to derive an imaging algorithm based on the hybrid processing in the time-domain and the wavenumber-domain. Specifically, we process the data in the wavenumber-domain along the z direction through utilizing the expansion of the spherical waves into the superposition of cylindrical and plane waves. In regard to the processing along the x and y directions, we employ the coherent summation with respect to the transmit and receive channels, which is appropriate due to the fewer antennas than those along the vertical direction.

First, to transform the data into the wavenumber-domain in the vertical direction, we apply the fast Fourier transform (FFT) on both sides of (1) with respect to z_T and z_R, respectively, then obtain,

$$s(\vec{r}_T, \vec{r}_R, k_{z_T}, k_{z_R}, k) = \iiint g(x, y, z) \mathcal{F}_{z_T}[e^{-jkR_T}]\mathcal{F}_{z_R}[e^{-jkR_R}]dxdydz. \tag{6}$$

The exponential terms of e^{-jkR_T} and e^{-jkR_R} in (6) are the phase terms of the free space Green's functions, whose Fourier transforms with respect to z_T and z_R can be, respectively, expressed as [43]

$$\mathcal{F}_{z_T}[e^{-jkR_T}] = e^{-j(k_{\rho T}\rho_T + k_{z_T} z)}, \tag{7}$$

$$\mathcal{F}_{z_R}[e^{-jkR_R}] = e^{-j(k_{\rho R}\rho_R + k_{z_R} z)}, \tag{8}$$

where

$$k_{\rho T} = \sqrt{k^2 - k_{z_T}^2}, \tag{9}$$

and

$$k_{\rho R} = \sqrt{k^2 - k_{z_R}^2}. \tag{10}$$

Substituting (7) and (8) in (6) yields

$$s(\vec{r}_T, \vec{r}_R, k_{z_T}, k_{z_R}, k) = \iiint g(x, y, z) e^{-j(k_{\rho_T}\rho_T + k_{z_T} z)} e^{-j(k_{\rho_R}\rho_R + k_{z_R} z)} dxdydz. \tag{11}$$

Defining the following relation,

$$k_z = k_{z_T} + k_{z_R}, \tag{12}$$

we further simplify (11) as,

$$s(\vec{r}_T, \vec{r}_R, k_{z_T}, k_{z_R}, k) = \iiint g(x, y, z) e^{-j(k_{\rho_T}\rho_T + k_{\rho_R}\rho_R)} e^{-jk_z z} dxdydz. \tag{13}$$

The integral over z can be expressed as a 1-D Fourier transform of $g(x, y, z)$, which then leads to,

$$s(\vec{r}_T, \vec{r}_R, k_{z_T}, k_{z_R}, k) = \iint g(x, y, k_z) e^{-j(k_{\rho_T}\rho_T + k_{\rho_R}\rho_R)} dxdy. \tag{14}$$

As mentioned above, we can achieve $g(x, y, k_z)$ through the time-domain processing. Before doing so, we should first obtain $g(x, y, k_{z_T}, k_{z_R})$ due to the existence of independent k_{z_T} and k_{z_R}, as follows,

$$g(x, y, k_{z_T}, k_{z_R}) = \iiint s(\vec{r}_T, \vec{r}_R, k_{z_T}, k_{z_R}, k) e^{jk_{\rho_T}\rho_T} e^{jk_{\rho_R}\rho_R} k d\vec{r}_T d\vec{r}_R dk. \tag{15}$$

This procedure can be realized using coherent summation with respect to all the possible transmit-receive pairs and frequencies. Clearly, the coherent accumulation expressed in (15) can be calculated for arbitrarily spaced $\vec{r}_T$ and $\vec{r}_R$, which makes the derived algorithm universal for multi-plane MIMO array with the arbitrary horizontal distribution of transmit-receive pairs.

Then, the next problem is to convert the 4-D $g(x, y, k_{z_T}, k_{z_R})$ into $g(x, y, k_z)$. Based on the relation in (12), $g(x, y, k_z)$ can be acquired by applying the proper dimension reduction to $g(x, y, k_{z_T}, k_{z_R})$. The specific process of the dimension reduction will be explained in the following subsection of the algorithm implementation. Finally, the 3-D reflectivity function $g(x, y, z)$ is obtained by simply applying a 1-D IFFT with respect to k_z. The imaging procedure can be summarized as,

$$\begin{aligned} g(x, y, z) &= \mathcal{F}_{k_z}^{-1}\{D_{4-3}[g(x, y, k_{z_T}, k_{z_R})]\} \\ &= \mathcal{F}_{k_z}^{-1}\{D_{4-3}[\iiint s(\vec{r}_T, \vec{r}_R, k_{z_T}, k_{z_R}, k) \\ &\quad e^{jk_{\rho_T}\rho_T} e^{jk_{\rho_R}\rho_R} k d\vec{r}_T d\vec{r}_R dk]\}, \end{aligned} \tag{16}$$

where $\mathcal{F}_{k_z}^{-1}$ indicates the 1-D IFFT with respect to k_z and D_{4-3} represents the dimension reduction from the 4-D data to a 3-D one.

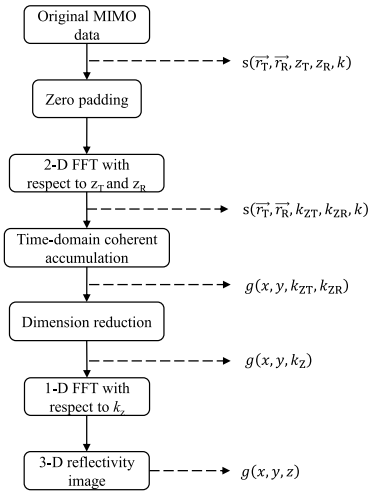

FIGURE 2. Block diagram of the hybrid time-wavenumber domain algorithm for multi-plane MIMO array.

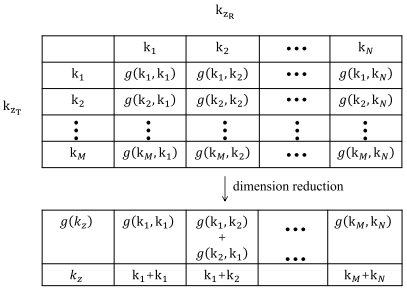

FIGURE 3. Illustration of the dimension reducing from $g(k_{z_T}; k_{z_R}; \cdots)$ to $g(k_z; \cdots)$.

B. ALGORITHM IMPLEMENTATION

This section deals with the practical implementation of the proposed hybrid time-wavenumber domain imaging algorithm. Based on the formulation in (16), the image reconstruction procedure can be separated into five sequential steps as shown in Fig. 2.

Zero padding is an indispensable step before applying 2-D FFT with respect to z_T and z_R. To successfully perform the dimension reduction, the discretization of k_{z_T} and k_{z_R} should be the same. Therefore, zero padding is applied to the undersampled antenna elements along the vertical direction, so that the following equation is satisfied [25],

$$\frac{1}{N_{z_T}\Delta_{z_T}} = \frac{1}{N_{z_R}\Delta_{z_R}}. \tag{17}$$

where Δ_{z_T} and Δ_{z_R} denote the sampling steps of the transmit and receive arrays along the vertical direction, and N_{z_T} and N_{z_R} are the points of 2-D FFT which transforms the data from (z_T, z_R) to (k_{z_T}, k_{z_R}) domain.

After the 2-D FFT operation, the data are multiplied by the corresponding exponential phase term $e^{jk_{\rho_T}\rho_T} e^{jk_{\rho_R}\rho_R}$. Then, $g(x, y, k_{z_T}, k_{z_R})$ can be easily obtained through the time-domain coherent accumulation according to (15).

To obtain $g(x, y, k_z)$, the dimension reduction should be applied to $g(x, y, k_{z_T}, k_{z_R})$ properly, which is shown in Fig. 3, where $g(x, y, k_{z_T}, k_{z_R})$ and $g(x, y, k_z)$ have been simplified as $g(k_{z_T}, k_{z_R})$ and $g(k_z)$ respectively for conciseness. Based on

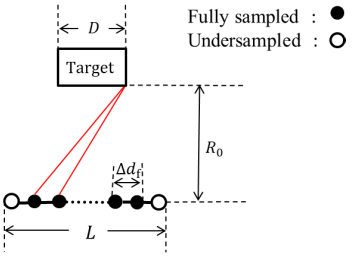

FIGURE 4. Illustration of sampling criteria for one side of the squared subarray.

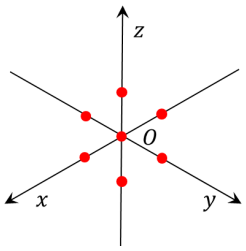

FIGURE 5. Target model.

(12), $g(k_z)$ can be obtained by adding all the data $g(k_{z_T}, k_{z_R})$ where the sum of k_{z_T} and k_{z_R} equals to k_z. Therefore, if the length of k_{z_T} and k_{z_R} are M and N respectively, the number of elements in $g(k_z)$ will be $M + N - 1$.

Finally, the reflectivity image $g(x, y, z)$ can be attained by simply applying the 1-D IFFT to $g(x, y, k_z)$.

C. INTER-ELEMENT SPACING

Next, we discuss the sampling requirements for the proposed MIMO array scheme. Each squared subarray can be divided into four sides with the same structure, as illustrated in Fig. 4. The sampling requirements for the inter-element spacings can be analyzed via using any one of them.

To avoid the image aliasing, the maximum phase difference between two adjacent transmit or receive antennas has to be less than π rad. So, the inter-element spacing for the fully sampled subarray should satisfy the following relation [25],

$$k\Delta d_f \frac{(L+D)/2}{\sqrt{(L+D)^2/4 + R_0^2}} \leq \pi, \tag{18}$$

where Δd_f denotes the spacing of two neighboring antennas of the fully sampled subarray, L denotes the length of the fully sampled subarray, D represents the maximal target dimension, and R_0 denotes the minimal distance from the subarray to the target center. Then, we obtain

$$\Delta d_f \leq \lambda_{\min} \frac{\sqrt{(L+D)^2/4 + R_0^2}}{L+D}, \tag{19}$$

where $\lambda_{\min}$ denotes the smallest wavelength of the working EM waves.

In regard to the undersampled subarray, there is no specific restriction on its spacing due to the fact that the final image is obtained by multiplication of the transmit and receive array patterns, as long as the target area can be uniformly illuminated or the reflected waves can be uniformly received. In this work, we set the elements of the undersampled subarray only at both ends of the straight fully sampled subarray, as shown in Fig. 4.

D. RESOLUTIONS

The imaging resolutions are determined by the span of the target spectrum along each dimension, which is related to the parameters including bandwidth, frequencies, antenna beamwidth, and angles subtended by the MIMO array.

First, we consider the cross-range resolution along the horizontal direction, which is given by,

$$\delta_x = \frac{\pi}{k_{x_{\max}}} = \frac{c}{4f_c \sin(\theta_x/2)}, \tag{20}$$

where $k_{x_{\max}}$ represents the maximum of the spatial frequency $k_x = k_\rho \sin\theta$, with θ denoting the angle between the wave vector $\vec{k}_\rho$ and the y direction, and f_c denotes the center frequency of the working EM waves. θ_x represents the minimum one between the antenna beamwidth and the angle subtended by the array along the horizontal direction.

Similarly, for the resolution along the vertical direction, we note from (12) that $k_{z_{\max}} = k_{z_{T\max}} + k_{z_{R\max}}$ with $k_{z_{T\max}} = k_{z_{R\max}} \approx \frac{2\pi f_c \sin(\theta_z/2)}{c}$. Hence, we have

$$\delta_z = \frac{\pi}{k_{z_{\max}}} = \frac{c}{4f_c \sin(\theta_z/2)}, \tag{21}$$

where $k_{z_{\max}}$ represents the maximum of spatial frequency k_z, and θ_z denotes the minimum one between the antenna beamwidth and the angle subtended by the array along the vertical direction.

Finally, the down-range resolution is easily given by,

$$\delta_y = \frac{c}{2B}, \tag{22}$$

where B represents the frequency bandwidth.

It is noteworthy that we just show the theoretical analysis of image resolutions without considering the influence of the antenna pattern. Readers can refer to [44] for more details about the effect of antenna pattern on the image resolutions in the near-field area.

III. RESULTS AND DISCUSSIONS

This section demonstrates the imaging performance of the proposed multi-plane MIMO array scheme and the corresponding imaging algorithm via numerical simulation and experimental results. To show the superiority of the proposed imaging technique, the state-of-the-art representative MIMO array schemes and imaging algorithms are used for comparisons. The algorithms were implemented on a computer platform with two E5-2687W CPUs.

A. COMPARISON OF ILLUMINATION UNIFORMITY OF THE TARGET AREA

In this subsection, the uniformity of wave illumination of the target area of the proposed multi-plane MIMO array is compared to that of the planar and cylindrical MIMO arrays

TABLE 1. Parameters of multi-plane, cylindrical and planar MIMO arrays.

Parameters	Value
Start frequency	30 GHz
Stop frequency	35 GHz
Number of frequency steps	51
Number of transmit antennas along the vertical direction	5
Number of receive antennas along the vertical direction	61
Interval of transmit antennas along the vertical direction	0.15 m
Interval of receive antennas along the vertical direction	0.01 m
Number of transmit antennas along the horizontal direction	79
Number of receive antennas along the horizontal direction	4
Angle interval of transmit antennas along the horizontal direction	1.47 °
Angle interval of receive antennas along the horizontal direction	38.11 °
Beamwidth of antenna elements	30 °

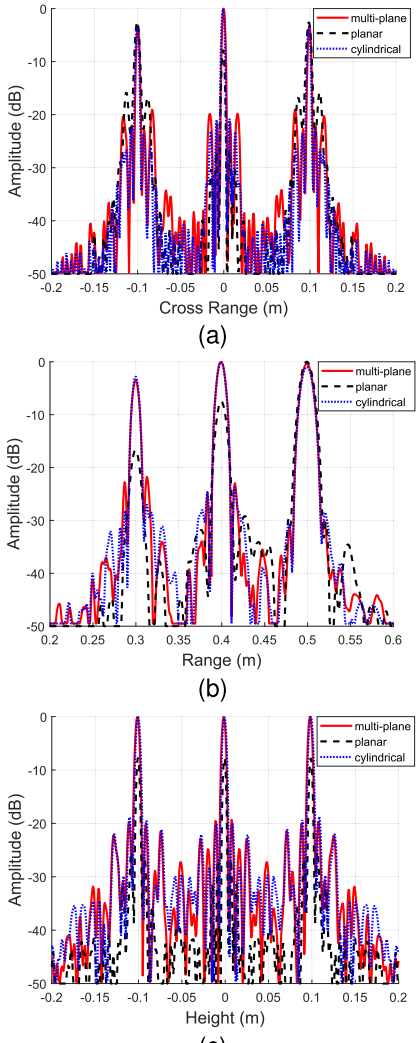

FIGURE 6. Comparison of imaging results between multi-plane, planar and cylindrical MIMO arrays in the (a) horizontal direction, (b) vertical direction, and (c) down-range direction.

by means of numerical simulations. The point targets under test are distributed along the three axes with a spacing of 0.1 m, as shown in Fig. 5. Here, we choose the three-plane MIMO array to balance the simplicity and demonstration of the multi-plane MIMO array. The minimum distance R_0 from the center scatterer to the multi-plane MIMO array is 0.4 m. The parameters of the multi-plane, planar, and cylindrical

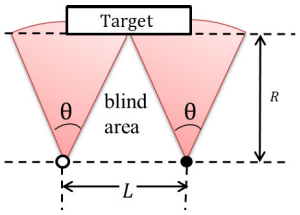

FIGURE 7. Illustration of antenna beamwidth and blind area.

TABLE 2. Comparison of amplitude attenuation.

	$R = 0.3$ m	$R = 0.4$ m	$R = 0.5$ m
Multi-plane array	-3.35 dB	0 dB	-0.56 dB
Cylindrical array	-2.71 dB	0 dB	-1.12 dB
Planar array	-15.72 dB	-7.40 dB	0 dB

MIMO arrays are listed in Table 1. The beams of the antenna element of these arrays are simulated by a sinc function whose main lobe is set to 30 °. Clearly, the vertical antenna configurations of the planar and cylindrical MIMO arrays are consistent with that of the multi-plane one, which allows them to maintain the same vertical resolution. To achieve the same horizontal resolution, the planar and cylindrical MIMO arrays maintain the same horizontal observation angle as that of the multi-plane one.

To ensure that the imaging results are only related to the array topologies, the BP algorithm is employed for the three schemes. Here, we only provide the 1-D imaging result slices passing through the center target along the three directions, as presented in Fig. 6. The three peaks of Fig. 6 (a), (b), and (c) represent the focusing magnitude of point targets distributed on the x, y, and z axes, respectively. Note that the magnitude uniformity of the targets of the proposed array and the cylindrical array along the cross-range and down-range directions is much better than that of the planar array, as shown in Figs. 6 (a) and (b), since the former two arrays can steer the antenna beams toward the target center along the horizontal plane. Also, as the target gets closer to the array, the amplitude will have more deterioration for the planar MIMO array in comparison with that of the multi-plane or the cylindrical arrays. The magnitude uniformity of the three types of arrays along the vertical direction is much similar to each other due to the same array structure, except for the image amplitudes of the planar array that are overall lower than those of the other two arrays since the best illuminated target by the planar array is the farthest one, not the three targets along the z axis. Fig. 7 provides an illustration of such a configuration. When the target is set at a distance smaller than R, it will not be fully covered by the transmit and receive antennas with spacing larger than L. The quantitative results of amplitude decay of the targets located on the y axis are shown in Table 2. Clearly, the planar MIMO array possesses the best focusing amplitude for the farthest target, while reaches the most severe amplitude decay of -15.72 dB for the nearest target. The multi-plane and cylindrical MIMO arrays show the best focusing performance for the center target. For the closest target, the amplitude decay of the multi-plane MIMO array is 0.64 dB

TABLE 3. Computatingal complexity analysis of the multi-plane MIMO hybrid time-wavenumber domain algorithm.

Operations	Computations (FLOPs)
2D FFT over the vertical dimension (zero padded)	$5N_f N_{\mathrm{h}}^2 N_{\mathrm{v}}^2 \log N_{\mathrm{v}}^2$
Time-domain coherent accumulation	$(C+1)N_x N_y N_f N_{\mathrm{h}} N_{\mathrm{v}}^2$
Dimension reduction	$2N_x N_y (N_{\mathrm{v}}-1)^2$
1D IFFT	$5N_x N_y N_z \log N_z$

TABLE 4. Computatingal complexity analysis of the cylindrical RMA.

Operations	Computations (FLOPs)
4D FFT over the vertical and horizontal dimension (zero padded)	$20N_f N_{\mathrm{h}}^2 N_{\mathrm{v}}^2 \log 4N_{\mathrm{v}}^2 N_{\mathrm{h}}^2$
Matched filtering	$24N_f N_{\mathrm{h}}^2 N_{\mathrm{v}}^2$
2-D IFFT over the horizontal dimension	$20N_f N_{\mathrm{h}}^2 N_{\mathrm{v}}^2 \log 4N_{\mathrm{h}}^2$
Dimension increase	-
2-D interpolations	$14(N_f N_{\mathrm{v}}^2 N_{\mathrm{h}} M_x M_y + M_x^2 M_y^2 N_{\mathrm{h}}^2)$
Dimension reduction	$2(M_x-1)^2 M_y^2 N_{\mathrm{h}}^2 + 2(2M_x-1)(M_y-1) + 2(2M_x-1)(2M_y-1)(N_{\mathrm{h}}-1)$
3-D IFFT	$5N_x N_y N_z \log N_x N_y N_z$

more than that of the cylindrical one, but 12.37 dB less than that of the planar MIMO array, which clearly demonstrates that the multi-plane and cylindrical MIMO array can achieve more uniform illumination than the planar one for the targets in the near-field due to their multi-view observations.

B. COMPARISON OF THE PROPOSED ARRAY SCHEME AND THE CYLINDRICAL MIMO ARRAY SCHEME

The proposed muti-plane MIMO array can offer a similar focusing performance to that of the cylindrical MIMO array according to the analysis in Section III-A. However, the cylindrical RMA [38] takes much time to process the data acquired by cylindrical MIMO array. In this subsection, we provide more comparisons of the proposed imaging algorithm with the approach presented in [38] in terms of resolution, peak-to-sidelobe level ratio (PSLR), and computation time.

First, we discuss the computation efficiency of the both algorithms using the floating-point operations (FLOPs) [45]. The total computational complexity of the proposed algorithm and that of the cylindrical RMA are listed in Table 3 and Table 4, respectively. The size of the reconstructed image is represented by $N_x \times N_y \times N_z$. N_f denotes the number of frequency samples and C represents the number of planar sub-apertures contained in the multi-plane array. N_h and N_v are the numbers of fully sampled antenna elements along the horizontal and vertical dimensions, respectively. In Table 4, as for the cylindrical RMA, M_x and M_y represent the numbers of frequency points after bilinear interpolation with respect to the horizontal and range dimensions, respectively. The most computationally intensive part of multi-plane MIMO hybrid time-wavenumber domain algorithm is the time-domain coherent accumulation. The higher computation complexity of the cylindrical RMA is due to the matched filtering and interpolations [38]. Thus, the computational load of the proposed algorithm and the cylindrical RMA can be approximately estimated by their highest order of computational complexity. Generally, to obtain a better imaging result, M_x and M_y are set comparably to N_x and N_y, respectively. Then the computation complexity of the cylindrical RMA is roughly $(13-C)N_f N_h N_v^2 M_x M_y + 16M_x^2 M_y^2 M_z^2$ more than that of the multi-plane MIMO hybrid time-wavenumber domain algorithm. To balance the focusing performance and system cost of the multi-plane MIMO array, the value of C is usually less than 13. Clearly, the multi-plane MIMO hybrid time-wavenumber domain algorithm is more efficient than the cylindrical RMA according to the above analysis.

TABLE 5. Parameters of multi-plane and cylindrical MIMO arrays.

Parameters	Value
Start frequency	27 GHz
Stop frequency	32 GHz
Number of frequency steps	15
Number of transmit antennas along the vertical direction	5
Number of receive antennas along the vertical direction	41
Interval of transmit antennas along the vertical direction	0.1 m
Interval of receive antennas along the vertical direction	0.01 m
Number of transmit antennas along the horizontal direction	41
Number of receive antennas along the horizontal direction	5
Angle interval of transmit antennas along the horizontal direction	0.38 °
Angle interval of receive antennas along the horizontal direction	3.8 °

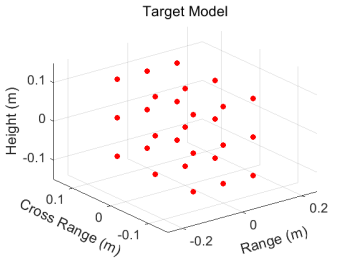

FIGURE 8. Target model for comparing the algorithms.

The imaging performance of the multi-plane MIMO hybrid time-wavenumber domain algorithm and the cylindrical RMA is demonstrated by the simulation as follows. In order to analyze the focusing performance of the algorithm independently, the influence of antenna beamwidth, which has already been discussed in Section III-A, is not considered here. The same parameters of the multi-plane MIMO array and the cylindrical one are listed in Table 5. The target model is shown in Fig. 8 with the distance from the target center to the multi-plane MIMO array being 1.5 m. According to the previous analysis, the theoretical down-range and cross-range (along the horizontal and vertical dimensions) resolutions are 3 cm and 1.92 cm, respectively.

The 2-D imaging result slices with respect to the horizontal-range, vertical-horizontal, and vertical-range planes are presented in Fig. 9. Although the multi-plane MIMO hybrid time-wavenumber domain algorithm has slight deteriorations in the focusing performance of down-range direction compared with the cylindrical RMA, the former can achieve the similar focusing performance to the latter in the horizontal and vertical directions.

Fig. 10 (a), (b), and (c) provide the 1-D imaging result slices passing through the target with the best focusing

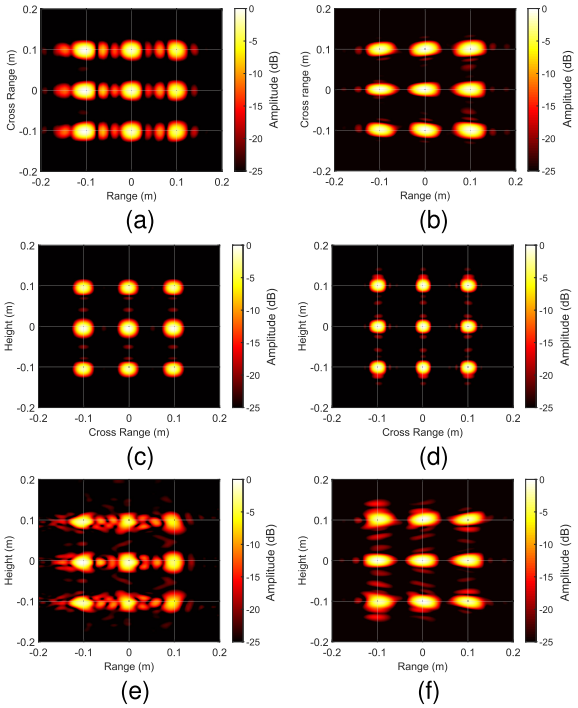

FIGURE 9. 2-D images with respect to the three coordinate planes by the multi-plane MIMO hybrid time-wavenumber domain algorithm: (a), (c), (e), and by the cylindrical MIMO array wavenumber-domain algorithm: (b), (d), and (f).

TABLE 6. Quantitative comparisons.

Performance parameters	theoretical	cylindrical RMA	proposed algorithm
Resolution in down-range direction	3 cm	3.08 cm	2.57 cm
Resolution in vertical direction	1.92 cm	2.13 cm	2.21 cm
Resolution in horizontal direction	1.92 cm	1.76 cm	2.15 cm
PSLR in the down-range direction	-	-16.77 dB	-12.99 dB
PSLR in vertical direction	-	-16.18 dB	-26.26 dB
PSLR in horizontal direction	-	-23.22 dB	-27.39 dB
Computation time	-	1500 s	194 s

magnitude along the horizontal, vertical, and down-range directions, respectively. The quantitative comparisons are presented in Table 6. Here, we take the 3 dB width of the point spread function as the resolution in the simulation. Since the theoretical resolutions are deduced based on the cube-shaped spatial spectrum, while the real spatial spectrum has a fan-shaped zone, the theoretical values and the simulated ones are slightly different. The resolution in the horizontal direction of the proposed algorithm is slightly inferior to that of the cylindrical RMA. However, the proposed algorithm exhibits better resolution in the down-range direction. The PSLR along the down-range direction of the proposed algorithm is 3.48 dB higher than that of the cylindrical RMA. However, the PSLR along the vertical direction of the proposed algorithm is 10.08 dB lower than that of the cylindrical RMA.

The main superiority of the proposed algorithm over the cylindrical RMA lies in the computation time, the former is 194 s, whereas the latter is approximately 1500 s. Therefore, compared with the cylindrical MIMO array imaging technique, the multi-plane MIMO hybrid time-wavenumber domain algorithm can achieve a great improvement in computational efficiency at the cost of only slight deteriorations of focusing performance. However, the computation time of the proposed algorithm is still quite long. Most of the time is taken by the process of time-domain coherent accumulation. This calls for the need to employ a fast approach, such as the parallel processing of the accumulated data, in the future. It is noteworthy that the array scale here is set to be smaller than that employed in the next subsection due to the fact that the computation time of the cylindrical RMA is too long if we utilize a larger array scale.

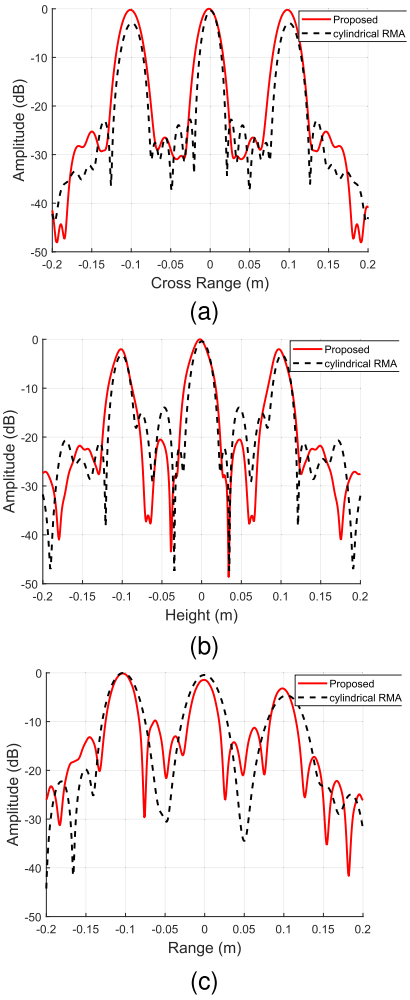

FIGURE 10. 1-D image corresponding to the (a) horizontal, (b) vertical, and (c) range dimensions.

C. COMPARISON OF THE IMAGING PERFORMANCE OF THE PROPOSED ALGORITHM AND BP

Next, for the multi-plane MIMO array, we compare the imaging performance of the proposed algorithm with that of the BP algorithm which is always taken as the golden standard. The BP algorithm can deal with any kind of array topologies, but its computational complexity is very high due to its full time-domain processing. Specifically, the computational complexity of BP is about $8(C+1)C_{\mathrm{vs}}N_xN_yN_zN_fN_hN_v$, where C_{vs} denotes the number of undersampled antenna elements along

TABLE 7. Simulation parameters of multi-plane MIMO array.

Parameters	Values
Start frequency	30 GHz
Stop frequency	35 GHz
Number of frequency steps	51
Number of planar subapertures	3
Number of transmit antennas along the vertical direction	5
Number of receive antennas along the vertical direction	61
Interval of transmit antennas along the vertical direction	0.15 m
Interval of receive antennas along the vertical direction	0.01 m
Number of transmit antennas along the horizontal direction	61
Number of receive antennas along the horizontal direction	4
Interval of transmit antennas in per planar subarray along the horizontal direction	0.01 m
Interval of receive antennas in per planar subarray along the horizontal direction	0.2 m
Minimum distance from the aperture to coordinate origin (R_0)	1 m

the vertical direction. Generally, since the value of C_{vs} should increase with the value of N_v to ensure a good focusing performance in the vertical direction, $\frac{C_{\text{vs}}}{N_v}$ can be approximately denoted as a constant k. By comparing with the complexity in Table 3, the differences in the computational complexities between the proposed algorithm and BP are roughly determined by the relation $\frac{8(C+1)C_{\text{vs}}N_xN_yN_zN_fN_hN_v}{(C+1)N_xN_yN_fN_hN_v^2} = 8kN_z$. Therefore, with the increase of N_z, the improvement of computational efficiency of the proposed algorithm will be more and more significant. This is mainly due to the different processing methods of the two algorithms for the target area along the vertical direction. The hybrid time-wavenumber domain algorithm processes the vertical pixels of targets in the wavenumber domain, while the BP algorithm needs to accumulate the time domain signal for each vertical pixel. Therefore, for the scenario with many pixels in the vertical dimension, such as the personnel imaging, the hybrid time-wavenumber domain algorithm can significantly save more time than the BP algorithm.

The specific parameters of multi-plane MIMO array in this simulation are listed in Table 7. The minimum distance R_0 from the multi-plane MIMO array to the target center is set to 1 m. The theoretical down-range and cross-range (along the horizontal and vertical dimensions) resolutions are 3 cm and 0.75 cm, respectively. The 3-D imaging results with a dynamic range of 25 dB are shown in Fig. 11, together with the results of BP as a benchmark for comparison. To view more details, the maximum value projected 2-D images with respect to the horizontal-range, vertical-horizontal, and vertical-range planes are respectively presented in Fig. 12. Fig. 13 depicts the 1-D image slices passing through the target with the best focusing magnitude along the three axes. Note that the imaging results of the proposed algorithm are slightly inferior to those of BP in the down-range direction but are similar in the vertical and horizontal directions.

Next, the quantitative comparisons with respect to resolution, PSLR, and computation time are provided in Table 8. Note that the resolutions of the proposed algorithm along the three directions are very close to those of BP. Although the

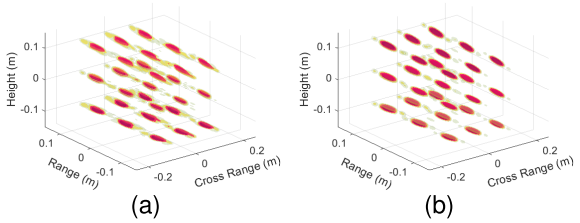

FIGURE 11. 3-D imaging results by (a) the proposed algorithm, and (b) BP.

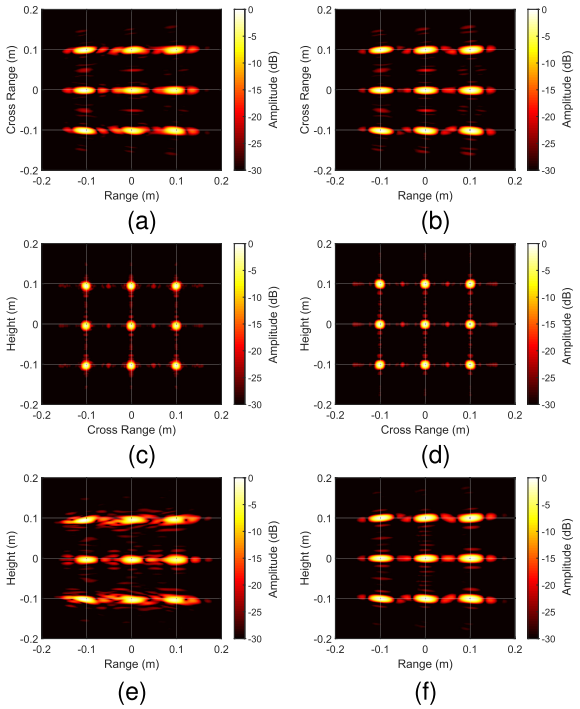

FIGURE 12. 2-D images with respect to the three coordinate planes by the proposed algorithm: (a), (c), (e), and by BP: (b), (d), and (f).

TABLE 8. Quantitative comparisons.

Performance parameters	theoretical	BP algorithm	Proposed algorithm
Resolution in down-range direction	3 cm	2.49 cm	2.36 cm
Resolution in vertical direction	0.75 cm	0.909 cm	0.938 cm
Resolution in horizontal direction	0.75 cm	0.85 cm	0.864 cm
PSLR in the down-range direction	-	-17.00 dB	-15.40 dB
PSLR in vertical direction	-	-25.05 dB	-26.78 dB
PSLR in horizontal direction	-	-24.56 dB	-24.77 dB
Computation time	-	1190 s	402.4 s

sidelobe level in the down-range direction of the proposed algorithm is 1.6 dB higher than that of BP, it exhibits similar or better performance in the horizontal and vertical directions. Both algorithms can achieve the sidelobe levels below -20 dB in the horizontal and vertical directions, which is mainly due to the multiplication of the beam patterns between the transmit and receive subarrays. Noticeably, the time required by the proposed algorithm is nearly one third of that of the BP algorithm which validates the superiority of the proposed method with regard to the computational complexity.

D. EXPERIMENTAL RESULTS

We constructed an experimental setup to further verify the imaging performance of the proposed imaging technique in

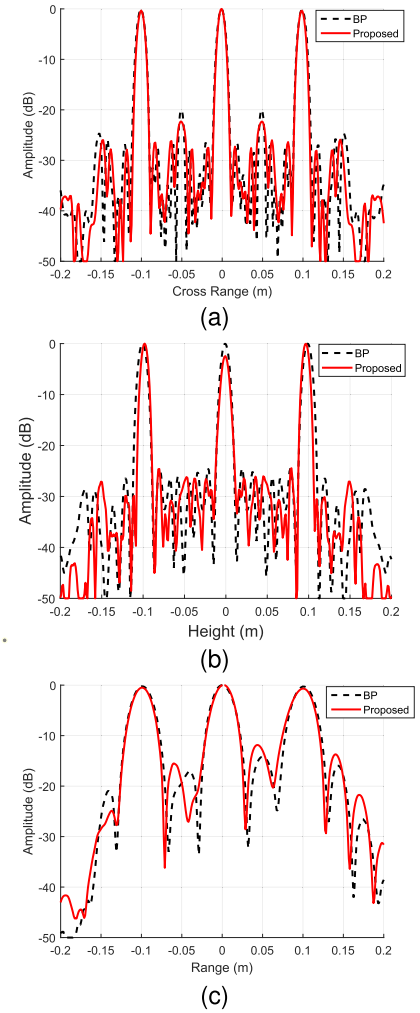

FIGURE 13. 1-D image corresponding to the (a) horizontal, (b) vertical, and (c) range dimensions.

TABLE 9. Equivalent multi-plane MIMO array parameters.

Parameters	Values
Number of planar subapertures	3
Number of transmit antennas along the vertical direction	5
Number of receive antennas along the vertical direction	61
Interval of transmit antennas along the vertical direction	0.15 m
Interval of receive antennas along the vertical direction	0.01 m
Number of transmit antennas along the horizontal direction	81
Number of receive antennas along the horizontal direction	6
Interval of transmit antennas in per planar subarray along the horizontal direction	0.01 m
Interval of receive antennas in per planar subarray along the horizontal direction	0.27 m
Angle between the adjacent planar subarrays along the horizontal direction (α)	24 °
Minimum distance from the aperture to coordinate origin (R_0)	0.7 m

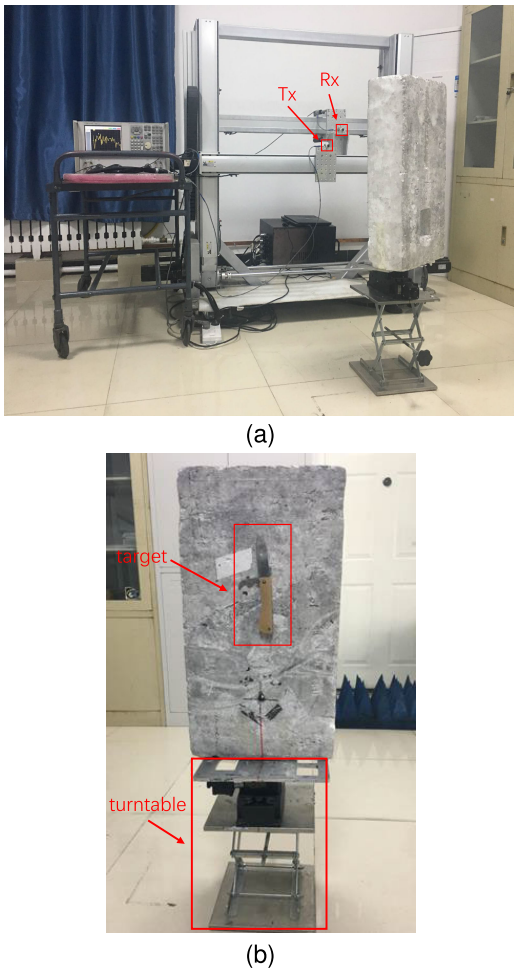

FIGURE 14. (a) Experimental scenario for generating the multi-plane MIMO array, and (b) photograph of a fruit knife fixed on the turntable.

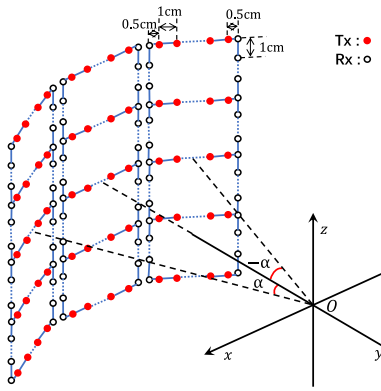

FIGURE 15. The equivalent multi-plane MIMO array topology in the experiment.

this subsection. The experimental scenario, shown in Fig. 14, includes the vector network analyzer (VNA), a planar scanning platform, and the target under test fixed on a turntable. The transmit and receive antennas are connected to the VNA, and fixed on two independently movable support beams of the planar scanning platform, respectively. The S_{21} parameters were measured as the scattered data from the target. The frequencies of the working EM waves vary from 30 GHz to 35 GHz with a step of 100 MHz. The target – a fruit knife as well as the turntable, is placed 0.7 m away from the planar scanning platform.

Due to the limitations of the experimental setup, we combine the planar scanning platform and the turntable to imitate the multi-plane MIMO array. Specifically, the turntable under the target is set to rotate at specified orientations, such as

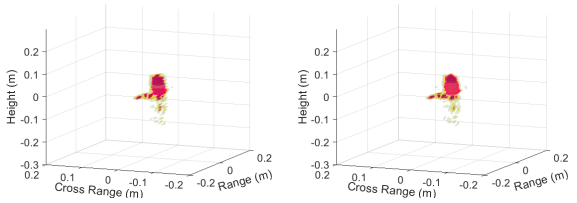

FIGURE 16. 3-D imaging results by (a) the proposed algorithm and (b) BP.

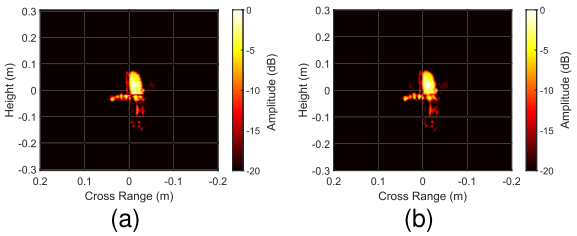

FIGURE 17. 2-D imaging results by (a) the proposed algorithm and (b) BP.

TABLE 10. Reconstruction performance.

Evaluation Indicator	BP algorithm	Proposed algorithm
entropy	0.2187	0.2192
Computation time	710 s	373 s

$-24°$, $0°$, and $24°$ in this example. With respect to each orientation, the transmit and receive antennas scan within a planar subaperture to form one of the three parts as illustrated in Fig. 15. Through this associated scanning, the multi-plane MIMO array scheme can be obtained. The parameters of the equivalent multi-plane MIMO array in this experiment are shown in Table 9. Note that only data acquisition within each planar subaperture can be acquired in this scheme which is different from the simulation. Fortunately, the proposed algorithm is suitable for generic multi-plane MIMO arrays with the arbitrary horizontal distribution of transmit-receive pairs since it performs coherent accumulation processing based on time-domain along the array dimension.

The reconstructed 3-D images are demonstrated in Fig. 16, with the result of BP as a benchmark. The corresponding 2-D images are shown in Fig. 17. The comparable imaging performance can be obtained by using the proposed algorithms and BP for the scheme in the experiment, which further indicates the effectiveness of the proposed array topology and the corresponding imaging algorithms. We note that there exist very slight fluctuations of the image amplitude of the proposed algorithm. It may be caused by the inaccurate positions among the adjacent transmit-receive antenna pairs since each antenna support beam has a finite size and as a result the transmit and receive antennas cannot be placed close enough in their appropriate adjacent positions. This introduces errors into the elevation processing using FFT; it, however, has no effect on the time-domain processing. This problem will not exist in practice when a real multi-plane MIMO array is employed.

Finally, we provide the quantitative comparison using entropy that has been successfully introduced to evaluate the quality of SAR images in [46]. It is defined as follows,

$$E = -\sum_{m=1}^{M}\sum_{n=1}^{N} \hat{g}(m,n)\ln[\hat{g}(m,n)], \tag{23}$$

where

$$\hat{g}(m,n) = \frac{|g(m,n)|^2}{\sum_{m=1}^{M}\sum_{n=1}^{N}|g(m,n)|^2} \tag{24}$$

represents the normalized image results, M and N represent the image size in the vertical and horizontal directions, and the $\ln(\cdot)$ function is used to calculate natural logarithm. Theoretically, the smaller entropy value indicates the better focusing performance of the image. Therefore, the entropy corresponding to Fig. 17 is calculated to evaluate the focusing property of the proposed algorithm, as shown in Table 10. The entropy results show that the proposed algorithm has a comparable imaging performance with that of BP. The computation time is also presented. Note that both algorithms take less time to process the experimental data than that to process the simulated one. This is mainly due to the fact that the transceiver antenna pair is limited in each segment of the multiplane MIMO array, which reduces the volume of data. The experimental results also show the proposed algorithm has strong generality and is suitable for various multiplane MIMO arrays with uniformly spaced antennas along the vertical direction. These quantitative indices further show that the proposed algorithm can achieve the same level of image quality as the BP algorithm but with a significantly lower computational cost.

IV. CONCLUSION

In this paper, a novel multi-plane MIMO array topology was presented, which can not only offer larger observation angles than the traditional planar MIMO arrays but also is much easier to fabricate than the cylindrical MIMO arrays. To improve the efficiency of image reconstruction using the proposed array, a hybrid time-wavenumber domain imaging algorithm was devised. The comparison results show that the proposed algorithm runs even faster than the wavenumber-domain algorithm for the cylindrical MIMO array. This is due to the fact that the wavenumber domain algorithm for MIMO arrays needs higher dimensional processing, which is time-consuming and requires more memory usage. Moreover, the hybrid time-wavenumber domain algorithm is suitable for various multiplane MIMO arrays with uniformly spaced antennas along the vertical direction, which demonstrates the versatility and wide applicability of the proposed algorithm. In terms of focusing performance, the proposed algorithm can achieve a similar image quality to that of BP algorithm, but with significantly lower computational complexity.

REFERENCES

[1] V. Venkatesh, L. Li, M. McLinden, M. Coon, G. M. Heymsfield, S. Tanelli, and H. Hovhannisyan, "A frequency diversity algorithm for extending the radar Doppler velocity Nyquist interval," *IEEE Trans. Aerosp. Electron. Syst.*, vol. 56, no. 3, pp. 2462–2470, Jun. 2020.

[2] A. Moreira, P. Prats-Iraola, M. Younis, G. Krieger, and I. P. K. Hajnsek, "A tutorial on synthetic aperture radar," *IEEE Geosci. Remote Sens. Mag.*, vol. 1, no. 1, pp. 6–43, May 2013.

[3] M. T. Ghasr, S. Kharkovsky, R. Bohnert, B. Hirst, and R. Zoughi, "30 GHz linear high-resolution and rapid millimeter wave imaging system for NDE," *IEEE Trans. Antennas Propag.*, vol. 61, no. 9, pp. 4733–4740, Sep. 2013.

[4] A. Och, P. A. Hölzl, S. Schuster, S. Scheiblhofer, D. Zankl, V. Pathuri-Bhuvana, and R. Weigel, "High-resolution millimeter-wave tomography system for nondestructive testing of low-permittivity materials," *IEEE Trans. Microw. Theory Techn.*, vol. 69, no. 1, pp. 1105–1113, Jan. 2021.

[5] S. Di Meo, P. F. Espín-López, A. Martellosio, M. Pasian, G. Matrone, M. Bozzi, G. Magenes, A. Mazzanti, L. Perregrini, F. Svelto, P. E. Summers, G. Renne, L. Preda, and M. Bellomi, "On the feasibility of breast cancer imaging systems at millimeter-waves frequencies," *IEEE Trans. Microw. Theory Techn.*, vol. 65, no. 5, pp. 1795–1806, May 2017.

[6] H. Arab, L. Chioukh, M. Dashti Ardakani, S. Dufour, and S. O. Tatu, "Early-stage detection of melanoma skin cancer using contactless millimeter-wave sensors," *IEEE Sensors J.*, vol. 20, no. 13, pp. 7310–7317, Jan. 2020.

[7] D. M. Sheen, D. L. McMakin, and T. E. Hall, "Three-dimensional millimeter-wave imaging for concealed weapon detection," *IEEE Trans. Microw. Theory Techn.*, vol. 49, no. 9, pp. 1581–1592, Sep. 2001.

[8] Y. Rodríguez-Vaqueiro, Y. Á. López, B. González-Valdes, J. Á. Martínez, F. Las-Heras, and C. M. Rappaport, "On the use of compressed sensing techniques for improving multistatic millimeter-wave portal-based personnel screening," *IEEE Trans. Antennas Propag.*, vol. 62, no. 1, pp. 494–499, Jan. 2014.

[9] D. Sheen, D. Mcmakin, and T. Hall, "Near-field three-dimensional radar imaging techniques and applications," *Appl. Opt.*, vol. 49, no. 19, pp. 83–93, 2010.

[10] J. Gao, Y. Qin, B. Deng, H. Wang, and X. Li, "Novel efficient 3D short-range imaging algorithms for a scanning 1D-MIMO Array," *IEEE Trans. Image Process.*, vol. 27, no. 7, pp. 3631–3643, Jul. 2018.

[11] M. L. Bryant, L. L. Gostin, and M. Soumekh, "3-D E-CSAR imaging of a T-72 tank and synthesis of its SAR reconstructions," *IEEE Trans. Aerosp. Electron. Syst.*, vol. 39, no. 1, pp. 211–227, Jan. 2003.

[12] H. Cetinkaya, S. Kueppers, R. Herschel, and N. Pohl, "Millimeter-wave MIMO array based on semi-circular topology," *IEEE Sensors J.*, vol. 20, no. 14, pp. 7740–7749, Mar. 2020.

[13] S. S. Ahmed, A. Schiess, and L.-P. Schmidt, "Near field mm-Wave imaging with multistatic sparse 2D-arrays," in *Proc. Eur. Radar Conf. (EuRAD)*, 2009, pp. 180–183.

[14] G. Gennarelli and F. Soldovieri, "Multipath ghosts in radar imaging: Physical insight and mitigation strategies," *IEEE J. Sel. Topics Appl. Earth Observ. Remote Sens.*, vol. 8, no. 3, pp. 1078–1086, Mar. 2015.

[15] P. Stoica, J. Li, and Y. Xie, "On probing signal design for MIMO radar," *IEEE Trans. Signal Process.*, vol. 55, no. 8, pp. 4151–4161, Aug. 2007.

[16] Y. Yang and R. S. Blum, "MIMO radar waveform design based on mutual information and minimum mean-square error estimation," *IEEE Trans. Aerosp. Electron. Syst.*, vol. 43, no. 1, pp. 330–343, Jan. 2007.

[17] D. Bleh, M. Rösch, M. Kuri, A. Dyck, A. Tessmann, A. Leuther, S. Wagner, B. Weismann-Thaden, H.-P. Stulz, M. Zink, M. Rießle, R. Sommer, J. Wilcke, M. Schlechtweg, B. Yang, and O. Ambacher, "*W*-band time-domain multiplexing FMCW MIMO radar for far-field 3-D imaging," *IEEE Trans. Microw. Theory Techn.*, vol. 65, no. 9, pp. 3474–3484, Sep. 2017.

[18] Y. Zhang, C. Zhu, S. Dong, Z. Gu, M. Balle, B. Zhang, C. Li, and L. Ran, "3-D motion imaging in a multipath coordinate space based on a TDM-MIMO radar sensor," *IEEE Trans. Microw. Theory Techn.*, vol. 68, no. 11, pp. 4642–4651, Nov. 2020.

[19] J. Shi, F. Wen, and T. Liu, "Nested MIMO radar: Coarrays, tensor modeling, and angle estimation," *IEEE Trans. Aerosp. Electron. Syst.*, vol. 57, no. 1, pp. 573–585, Feb. 2021.

[20] X. F. Zhang, L. Y. Xu, L. Xu, and D. Z. Xu, "Direction of departure (DOD) and direction of arrival (DOA) estimation in MIMO radar with reduced-dimension MUSIC," *IEEE Commun. Lett.*, vol. 14, no. 12, pp. 1161–1163, Dec. 2010.

[21] I. Bekkerman and J. Tabrikian, "Target detection and localization using MIMO radars and sonars," *IEEE Trans. Signal Process.*, vol. 54, no. 10, pp. 3873–3883, Oct. 2006.

[22] S.-Y. Jeon, S. Kim, J. Kim, S. Kim, S. Shin, M. Kim, and M.-H. Ka, "W-band FMCW MIMO radar system for high-resolution multimode imaging with time- and frequency-division multiplexing," *IEEE Trans. Geosci. Remote Sens.*, vol. 58, no. 7, pp. 5042–5057, Jul. 2020.

[23] S. W. Smith, H. G. Pavy, and O. T. Von Ramm, "High-speed ultrasound volumetric imaging system. I. Transducer design and beam steering," *IEEE Trans. Ultrason., Ferroelectr., Freq. Control*, vol. 38, no. 2, pp. 100–108, Mar. 1991.

[24] S. S. Ahmed, A. Schiessl, and L.-P. Schmidt, "A novel fully electronic active real-time imager based on a planar multistatic sparse array," *IEEE Trans. Microw. Theory Techn.*, vol. 59, no. 12, pp. 3567–3576, Dec. 2011.

[25] X. Zhuge and A. G. Yarovoy, "Three-dimensional near-field MIMO array imaging using range migration techniques," *IEEE Trans. Image Process.*, vol. 21, no. 6, pp. 3026–3033, Jun. 2012.

[26] T. Fromenteze, O. Yurduseven, F. Berland, C. Decroze, D. R. Smith, and A. G. Yarovoy, "A transverse spectrum deconvolution technique for MIMO short-range Fourier imaging," *IEEE Trans. Geosci. Remote Sens.*, vol. 57, no. 9, pp. 6311–6324, Apr. 2019.

[27] Z. Wang, X. Tian, T. Chang, and H.-L. Cui, "Phase-based range-enhanced millimeter-wave imaging technique for multistatic planar array," *IEEE Trans. Microw. Theory Techn.*, vol. 70, no. 3, pp. 1882–1895, Mar. 2022.

[28] T. Kato, H. Yamada, and H. Mori, "Experimental study on 3D imaging using millimeter-wave non-uniform 2D-MIMO radar," in *Proc. Int. Symp. Antennas Propag. (ISAP)*, 2022, pp. 231–232.

[29] J. Wang, P. Aubry, and A. Yarovoy, "3-D short-range imaging with irregular MIMO arrays using NUFFT-based range migration algorithm," *IEEE Trans. Geosci. Remote Sens.*, vol. 58, no. 7, pp. 4730–4742, Jan. 2020.

[30] J. Zhou, R. Zhu, G. Jiang, L. Zhao, and B. Cheng, "A precise wavenumber domain algorithm for near range microwave imaging by cross MIMO array," *IEEE Trans. Microw. Theory Techn.*, vol. 67, no. 4, pp. 1316–1326, Apr. 2019.

[31] Y. Álvarez, Y. Rodriguez-Vaqueiro, B. Gonzalez-Valdes, S. Mantzavinos, C. M. Rappaport, F. Las-Heras, and J. A. Martínez-Lorenzo, "Fourier-based imaging for multistatic radar systems," *IEEE Trans. Microw. Theory Techn.*, vol. 62, no. 8, pp. 1798–1810, Aug. 2014.

[32] W. F. Moulder, J. D. Krieger, J. J. Majewski, C. M. Coldwell, H. T. Nguyen, D. T. Maurais-Galejs, T. L. Anderson, P. Dufilie, and J. S. Herd, "Development of a high-throughput microwave imaging system for concealed weapons detection," in *Proc. IEEE Int. Symp. Phased Array Syst. Technol. (PAST)*, 2016, pp. 1–6.

[33] Leidos. *Provision 2*. [Online]. Available: https://www.leidos.com/markets/aviation/security-detection/aviation-checkpoint/people-screening

[34] S. Wu, H. Wang, C. Li, X. Liu, and G. Fang, "A modified Omega-K algorithm for near-field single-frequency MIMO-arc-array-based azimuth imaging," *IEEE Trans. Antennas Propag.*, vol. 69, no. 8, pp. 4909–4922, Jan. 2021.

[35] H. Eyal and R. Daisy, "Three dimnesional real time ultra-wide band whole body imaging system," in *Proc. IEEE Radar Conf.*, May 2012, pp. 0022–0027.

[36] L. Jaime, M. T. Ghasr, M. López-Portugués, F. Las-Heras, and R. Zoughi, "Real-time multiview SAR imaging using a portable microwave camera with arbitrary movement," *IEEE Trans. Antennas Propag.*, vol. 66, no. 12, pp. 7305–7314, Dec. 2018.

[37] S. Li, S. Wang, Q. An, G. Zhao, and H. Sun, "Cylindrical MIMO array-based near-field microwave imaging," *IEEE Trans. Antennas Propag.*, vol. 69, no. 1, pp. 612–617, Jan. 2021.

[38] S. Li, S. Wang, M. G. Amin, and G. Zhao, "Efficient near-field imaging using cylindrical MIMO arrays," *IEEE Trans. Aerosp. Electron. Syst.*, vol. 57, no. 6, pp. 3648–3660, Dec. 2021.

[39] S. Wang, S. Li, G. Zhao, and M. G. Amin, "Efficient wavenumber domain processing for near-field imaging with polyline arrays," *IEEE Trans. Microw. Theory Techn.*, vol. 70, no. 10, pp. 4544–4555, Oct. 2022.

[40] S. Wang, S. Li, Q. An, G. Zhao, and H. Sun, "Near-field millimeter-wave imaging via arrays in the shape of polyline," *IEEE Trans. Instrum. Meas.*, vol. 71, pp. 1–17, 2022.

[41] M. D. Desai and W. K. Jenkins, "Convolution backprojection image reconstruction for spotlight mode synthetic aperture radar," *IEEE Trans. Image Process.*, vol. 1, no. 4, pp. 505–517, Oct. 1992.
[42] P. M. Morse and H. Feshbach, *Methods of Theoretical Physics*. New York, NY, USA: McGraw-Hill, 1953.
[43] M. Soumekh, "Reconnaissance with slant plane circular SAR imaging," *IEEE Trans. Image Process.*, vol. 5, no. 8, pp. 1252–1265, Aug. 1996.
[44] C. Liu, M. T. A. Qaseer, and R. Zoughi, "Influence of antenna pattern on synthetic aperture radar resolution for NDE applications," *IEEE Trans. Instrum. Meas.*, vol. 70, pp. 1–11, 2021.
[45] G. K. M. Yano, J. D. Penn, and A. T. Patera, *Numerics and Programming: For Mechanical Engineers*. Cambridge, MA, USA: MIT OpenCourseWare, 2013.
[46] T. Zeng, R. Wang, and F. Li, "SAR Image autofocus utilizing minimum-entropy criterion," *IEEE Geosci. Remote Sens. Lett.*, vol. 10, no. 6, pp. 1552–1556, Nov. 2013.

GUANGNAN XING was born in Datong, Shanxi, China, in 1994. He received the B.S. degree in communication engineering from Beijing Information Science and Technology University, Beijing, China, in 2017. He is currently pursuing the Ph.D. degree with the Beijing Key Laboratory of Millimeter Wave and Terahertz Technology, Beijing Institute of Technology, Beijing.

His research interests include radar signal processing and terahertz imaging technology.

SHIYONG LI (Senior Member, IEEE) received the B.S. degree in electrical engineering from Shandong University, Jinan, China, in 2002, and the Ph.D. degree in electromagnetic field and microwave technology from the Beijing Institute of Technology, Beijing, China, in 2008.

From 2009 to 2010, he was a Postdoctoral Researcher with the School of Electronics Engineering and Computer Science, Peking University, Beijing. Since 2010, he has been with the faculty of the Beijing Institute of Technology, where he is currently an Associate Professor. He was a Visiting Research Scholar with the Center for Advanced Communications, Villanova University, Villanova, PA, USA, from September 2017 to September 2018. His current research interests include microwave imaging and radar indoor monitoring.

AHMAD HOORFAR (Life Fellow, IEEE) received the B.S. degree in electronics engineering from the University of Tehran, Tehran, Iran, in 1975, and the M.S. and Ph.D. degrees in electrical engineering from the University of Colorado at Boulder, Boulder, CO, USA, in 1978 and 1984, respectively.

He is currently a Professor of electrical and computer engineering, the Director of the Antenna Research Laboratory, and the Program Director of the EE Department's Graduate Admission and Advising, Villanova University, Villanova, PA, USA. Before joining Villanova, in 1988, he was a Postdoctoral Research Fellow with the Electromagnetics Laboratory, University of Colorado, from 1984 to 1986; and a Research Faculty with the NSF Research Center for Microwave/Millimeter-Waves Computer-Aided Design, Boulder, from 1986 to 1988. He spent his sabbatical leaves in 2002 and 2009 with NASA's Jet Propulsion Laboratory (JPL), Pasadena, CA, USA, where he contributed to the development of various global optimization techniques for the design of feed horns and antennas for NASA' deep space communication network. His research interests include electromagnetic field theory, electrically small and ultra-wideband antennas, metamaterials, metasurfaces, microwave sensing and imaging, radar systems, and evolutionary computational methods.

Dr. Hoorfar is a member of the Franklin Institute's Committee on Science and the Arts and the International Union of Radio Science (URSI), Commission B. In 1995, he was a recipient of the Philadelphia Section IEEE Chapter of the Year Award for his leadership in chairing the AP/MTT Joint Chapter (1993–1995). He was also a recipient of the Villanova University's Outstanding Faculty Research Scholar Award, in 2007. He was the General Chair and an Organizer of the 12th and 13th Benjamin Franklin Symposium in Microwave and Antenna Technology, in 1994 and 1995, respectively, and a Co-Organizer of the 22nd Antenna Measurement Technique Association (AMTA) Symposium, in 2000. He was a reviewer of various IEEE and other technical publications on antennas and microwaves in the last 30 years. He was also on the technical program committees of numerous international symposiums and conferences, including the IEEE AP-S, IEEE Aerospace, IEEE Radio and Wireless, IEEE Radar Conference, International Union of Radio Science (URSI), and Progress in Electromagnetic Research Symposium. He has organized numerous special sessions and was an invited speaker at various international symposiums in the areas of his research interest. He is currently a Distinguished Lecturer of the IEEE Antennas and Propagation Society (AP-S).

QIANG AN received the B.E., M.S., and Ph.D. degrees from the Department of Biomedical Engineering, Fourth Military Medical University, Xi'an, China, in 2012, 2015, and 2019, respectively.

He was with the Antenna Research Laboratory, Center for Advanced Communication, Villanova University, Villanova, PA, USA, as a Joint Training Ph.D. Student under the supervision of Dr. Ahmad Hoorfar, from February 2017 to September 2018. His research interests include through-the-wall radar imaging, ground-penetrating radar imaging, and radar indoor monitoring.

GUOQIANG ZHAO received the B.S. and M.S. degrees in electrical engineering and the Ph.D. degree in electromagnetic field and microwave technology from the Beijing Institute of Technology, Beijing, China, in 1994, 2004, and 2013, respectively.

He is currently an Associate Professor with the School of Information and Electronics, Beijing Institute of Technology. His research interests include radar signal processing, polarimetric information processing, microwave/millimeter-wave circuits and systems, and multipolarimetric antenna technology.